GFZ

Helmholtz-Zentrum
POTSDAM

Originally published as:

Images of the magnetotelluric apparent resistivity tensor

Ute Weckmann, Oliver Ritter and Volker Haak

GeoForschungsZentrum Potsdam, Telegrafenberg, D-14473 *Potsdam, Germany*

SUMMARY

We present a method for converting the magnetotelluric (MT) impedance tensor into an apparent resistivity tensor. The inclusion of anisotropic permittivity and conductivity into Maxwell's equations leads to a tensor expression for the propagation constant. To solve Maxwell's equations we assume exponentially decreasing electric fields in the vertical direction, which implies that the subsurface is regarded as homogeneous but anisotropic. This approach effectively makes use of an anisotropic substitute model, in which contrasts and strike directions of conductivity anomalies are transformed into equivalent amounts and directions of anisotropy. We call this method propagation number analysis (PNA). Rotationally invariant parameters calculated from the resistivity tensor are physically meaningful quantities that are directly applicable to imaging methods. Imaging results of PNA are compared with Egger's eigenstate analysis and LaTorraca's singular-value decomposition method using synthetic data from 3-D MT modelling. With PNA, we obtain a comprehensive image of the subsurface that uniquely images structural details of the anomalies. Contrary to other methods, the results of PNA are stable and significant under extreme 3-D conditions. Application of PNA to MT data from the Waterberg Fault in Namibia unravels a complicated 3-D impedance and reveals a clear correlation between the resistivity tensor and the surface geology.

Key words: apparent resistivity tensor, imaging method, invariants, magnetotelluric.

1 INTRODUCTION

The magnetotelluric (MT) impedance tensor reflects the 3-D distribution of magnetic and electric field variations within the Earth. MT practitioners attempt to determine the electrical conductivity structure of the subsurface by interpreting the impedance tensor as a function of position and frequency. For practical reasons we are often limited to 2-D modelling of the data, which means that the diagonal components of the impedance tensor are not considered in the interpretation. Eggers (1982) presented an approach for analysing impedances using an eigenstate parametrization, which uses all elements of the impedance tensor. His eigenstate formulation implies that electric and magnetic field polarizations are always orthogonal. This, however, is not necessarily true in a complex geoelectric environment. The singular-value decomposition (SVD) introduced by LaTorraca *et al.* (1986) overcomes this obstacle. Both methods result in sets of eigenvalues and eigenvectors (characteristic vectors). Their graphical presentation shows the orientation of the electromagnetic field defined by the principal directions of the polarization ellipses. Plots of the polarization ellipses thus provide geometrical insight into the 3-D information contained in the impedance tensor.

Another approach utilizing all four elements of the impedance tensor is the analysis of invariants. Invariant quantities are independent of the coordinate system and are most suitable to illustrate the internal structure of the impedance tensor. Fischer & Masero (1994) argued that a four-element complex tensor should possess eight real

invariants. Weaver *et al.* (2000) identified seven independent invariants. The algebraic relations between the various invariants were also examined systematically by Szarka & Menvielle (1997). Several authors have suggested that these tensor invariants can be presented as Mohr circles in the complex plane (Lilley 1993; Weaver *et al.* 2000). Images of the invariants, for example as plots in the horizontal plane for a certain frequency, result in seven different views of tensor properties. Their relation to physical properties of the subsurface is not always obvious.

Over the last few years tensor decomposition methods (Bahr 1991; Smith 1995; McNeice & Jones 2001, and references therein) have been widely used to condition the impedance tensor for subsequent 2-D interpretation. The basic idea is to decompose the impedance tensor into a 2-D complex tensor and a frequency-independent real distortion matrix. The complex tensor is related to a so-called regional conductivity structure, whereas the real matrix represents the galvanic response of small-scale, local heterogeneities. Upon decomposition, the regional tensor is generally interpreted using 2-D (inversion) modelling programs. The resulting conductivity model depends strongly on the validity of the galvanic assumption. It is often difficult to decide, however, to what extent small-scale and regional structures are connected by inductive coupling (Lezaeta & Haak 2003).

Imaging methods provide a different approach to understanding the conductivity distribution of the subsurface. They are based upon a direct conversion of measured data into physically meaningful

properties. The method described in this paper is comparable to the presentation of an apparent resistivity tensor introduced by Caldwell & Bibby (1998) for transient electromagnetics (TEM). Caldwell & Bibby present invariants of the measured resistivity tensor in form of ellipses, which was proposed earlier by Bibby (1986). In contrast with TEM or DC geoelectric sounding methods, however, we do not measure a resistivity tensor in MT. Upon taking the absolute values of the impedance to derive apparent resistivities, we lose the tensor character of our observations (see Appendix A). A direct application of this method to MT is therefore not straightforward but requires some considerations.

2 USING PROPAGATION NUMBER ANALYSIS TO OBTAIN AN APPARENT RESISTIVITY TENSOR IN MAGNETOTELLURICS

The method presented here was inspired by an internal report by Reilly (1979) on anisotropy tensors in magnetotelluric interpretation, which describes a theoretical concept formulated in terms of tensor algebra. An application to MT was demonstrated by Caldwell *et al.* (1998). In this section, we develop an alternative formulation of the problem, which should be more familiar for the MT community. Additionally, it more clearly shows the limitations of the method.

Below, we develop a true resistivity tensor by means of a substitute anisotropic half-space, which generates the same impedance tensor as the observed one. The commonly used MT apparent resistivity

$$\rho_{a,ij} = \frac{\mu_0}{2\pi f} |Z_{ij}|^2 \tag{1}$$

with i, $j = x$, y and frequency f, is not a tensor as shown in Appendix A. As a function of rotation the apparent resistivity is therefore not suitable for imaging properties of the MT impedance.

In MT a second-order tensor connects the electric and magnetic fields represented by the impedance $\boldsymbol{Z}$ or its inverse, the admittance tensor $\boldsymbol{Y}$:

$$\mathbf{B} = \mu \mathbf{H} = \hat{\boldsymbol{Y}} \mathbf{E} = \begin{pmatrix} Y_{xx} E_x + Y_{xy} E_y \\ Y_{yx} E_x + Y_{yy} E_y \end{pmatrix}, \tag{2}$$

where $\mathbf{B}$ is the magnetic flux density [T], $\mathbf{H}$ is the magnetic field intensity [A m^{-1}] $\mathbf{E}$ is the electric field intensity [V m^{-1}] and μ is the relative magnetic permeability of the medium [T m A^{-1}]. This tensor relation between electric and magnetic fields originates from Maxwell's equations. Assuming a harmonic time dependence proportional to $e^{i\omega t}$, the electric and magnetic fields take the following form:

$$\nabla \times \mathbf{E} = -i\omega \mathbf{B} \tag{3}$$

$$\nabla \times \mathbf{H} = \mathbf{j} + i\omega \mathbf{D}, \tag{4}$$

where $\mathbf{D}$ is the electric displacement [C m^{-2}], $\mathbf{j}$ is the current density [A m^{-2}] and ω is the angular frequency [Hz]. To transform Ampère's law (4) into a tensor relationship requires anisotropic permittivity ϵ [F m^{-1}] and conductivity σ [S m^{-1}]. This means that both parameters must be promoted from scalars to tensors. For physically realizable materials the tensors $\hat{\epsilon}$ and $\hat{\sigma}$ are symmetric (Negi & Saraf 1989). Using the material parameters for anisotropic media we can rewrite Maxwell's equations:

$$\nabla \times \mathbf{E} = -i\omega \mu \mathbf{H} \tag{5}$$

$$\nabla \times \mathbf{H} = \hat{\boldsymbol{\sigma}} \mathbf{E} + i\omega \hat{\epsilon} \mathbf{E}. \tag{6}$$

Multiplying Ampère's law by $i\omega\mu$ we can combine the right-hand side of eq. (6), thereby introducing the propagation constant γ in a similar way as in the general form of the Helmholtz equation:

$$\begin{aligned} -i\omega\mu\nabla \times \mathbf{H} &= -i\omega\mu(\hat{\boldsymbol{\sigma}} + i\omega\hat{\epsilon})\mathbf{E} \\ &= -\omega\mu(i\hat{\boldsymbol{\sigma}} - \omega\hat{\epsilon})\mathbf{E} \\ &= -\hat{\gamma}\mathbf{E}. \end{aligned} \tag{7}$$

The propagation constant $\hat{\gamma}$ is equivalent to the square of the wavenumber multiplied by $\sqrt{-1}$. Obviously though, $\hat{\gamma}$ is not a constant quantity. We therefore referring to $\hat{\gamma}$ as the propagation number analogue to the term wavenumber.

Replacing the magnetic field $\mathbf{H}$ with $\hat{\boldsymbol{Y}}\mathbf{E}$ in eqs (7) and (5), we obtain equations only dependent on the electric field $\mathbf{E}$,

$$-i\omega\nabla \times \hat{\boldsymbol{Y}}\mathbf{E} = -\hat{\gamma}\mathbf{E} \tag{8}$$

$$\nabla \times \mathbf{E} = -i\omega\hat{\boldsymbol{Y}}E. \tag{9}$$

To solve these equations we assume an exponentially decreasing electric field in the z direction (vertical). Formally, this is equivalent to the general solution of the wave equation for a vertically downward-propagating plane wave but neglecting the term describing the upward-propagating part. This solution implies that the subsurface is regarded as homogeneous but anisotropic in terms of conductivity and permittivity. In this case all spatial derivatives in the x and y directions are zero. Furthermore, a restriction to purely azimuthal anisotropy is justified as in MT we have no sensitivity to the vertical conductivity component.

Using above assumptions, Faraday's and Ampère's laws eqs (9) and (7) can be written as

$$\nabla \times \begin{pmatrix} E_x \\ E_y \\ 0 \end{pmatrix} = \begin{pmatrix} -\dfrac{\partial}{\partial z}E_y \\ \dfrac{\partial}{\partial z}E_x \\ 0 \end{pmatrix} = -i\omega \begin{pmatrix} Y_{xx}E_x + Y_{xy}E_y \\ Y_{yx}E_x + Y_{yy}E_y \\ 0 \end{pmatrix} \tag{10}$$

$$i\omega \begin{pmatrix} -\dfrac{\partial}{\partial z}(Y_{yx}E_x + Y_{yy}E_y) \\ \dfrac{\partial}{\partial z}(Y_{xx}E_x + Y_{xy}E_y) \\ 0 \end{pmatrix} = -\hat{\gamma} \begin{pmatrix} E_x \\ E_y \\ 0 \end{pmatrix}. \tag{11}$$

In the following discussion, we omit the vanishing z component of electric fields for clarity. The admittance tensor is not a function of depth, hence $\frac{\partial}{\partial z}(Y_{xy}E_x) = Y_{xy}\frac{\partial}{\partial z}E_x$, and we can substitute the partial derivatives of E_x and E_y using the right-hand side of eq. (10),

$$-(i\omega)^2 \begin{pmatrix} -Y_{yx}(Y_{yx}E_x + Y_{yy}E_y) + Y_{yy}(Y_{xx}E_x + Y_{xy}E_y) \\ Y_{xx}(Y_{yx}E_x + Y_{yy}E_y) - Y_{xy}(Y_{xx}E_x + Y_{xy}E_y) \end{pmatrix}$$
$$= -\hat{\gamma} \begin{pmatrix} E_x \\ E_y \end{pmatrix}. \tag{12}$$

The vector on the left-hand side of this equation can be decomposed into the dot product of a 2×2 matrix (containing combinations of all entries of the admittance tensor) and an electric field vector,

$$-\omega^2 \begin{pmatrix} Y_{yy}Y_{xx} - Y_{yx}Y_{yx} & Y_{yy} \cdot (Y_{xy} - Y_{yx}) \\ Y_{xx} \cdot (Y_{yx} - Y_{xy}) & Y_{yy}Y_{xx} - Y_{xy}Y_{xy} \end{pmatrix} \cdot \begin{pmatrix} E_x \\ E_y \end{pmatrix}$$
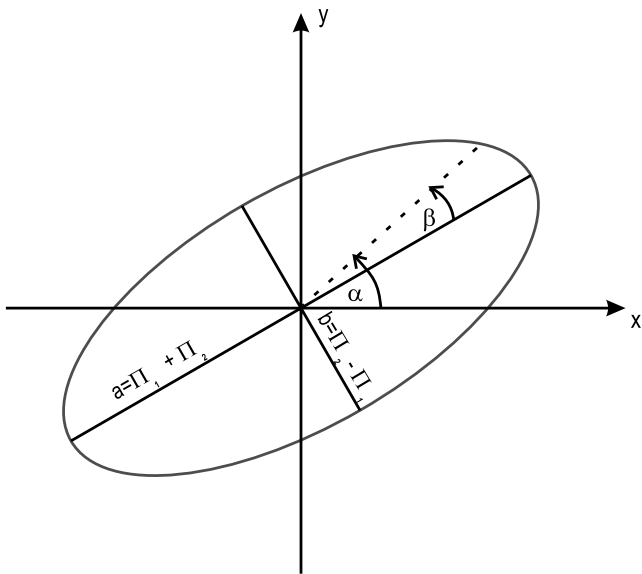$$= \hat{\gamma} \begin{pmatrix} E_x \\ E_y \end{pmatrix}. \tag{13}$$

Figure 1. Construction of an apparent resistivity ellipse: Π_1 and Π_2 define the lengths of the major and minor axes. These quantities, along with the rotation angles α and β are obtained by separating the apparent resistivity tensor into symmetric and asymmetric parts (Bibby 1986).

The tensor γ takes the following form:

$$\begin{pmatrix} \gamma_{xx} & \gamma_{xy} \\ \gamma_{yx} & \gamma_{yy} \end{pmatrix} = -\omega^2 \begin{pmatrix} Y_{yy}Y_{xx} - Y_{yx}Y_{yx} & Y_{yy} \cdot (Y_{xy} - Y_{yx}) \\ Y_{xx} \cdot (Y_{yx} - Y_{xy}) & Y_{yy}Y_{xx} - Y_{xy}Y_{xy} \end{pmatrix}. \quad (14)$$

The propagation number is defined as $\hat{\gamma} = -\omega^2 \mu \hat{\epsilon} + i\omega\mu\hat{\sigma}$. The real part of this complex tensor is a function the permittivity $\hat{\epsilon}$, whereas the imaginary part is dependent upon the conductivity $\hat{\sigma}$. Thus, the

MT apparent resistivity tensor is

$$\hat{\varrho} = \hat{\sigma}^{-1} = \mu\omega[\mathrm{Im}(\hat{\gamma})]^{-1}. \quad (15)$$

The real and imaginary parts of complex tensors are also tensors. Our newly obtained quantity $\hat{\varrho}$ is therefore a true tensor, in contrast to the apparent resistivity matrix derived by taking the squared absolute values of Z_{ij} (see eq. 1 and Appendix A).

In this paper, we are interested in developing a method for imaging the conductivity distribution of the subsurface. We therefore concentrate on the interpretation of the resistivity tensor as defined in eq. (15). It should be noted, however, that the real part of $\hat{\gamma}$ is related to the permittivity tensor $\hat{\epsilon}$. The electrical permittivity is typically not considered in MT applications because it is associated with vanishing displacements currents. In spite of this, the real part of $\hat{\gamma}$ contains some aspects of the admittance tensor and a more systematic inspection of $\hat{\epsilon}$ would be interesting but is beyond the scope of this paper.

In the following, we refer to this method as propagation number analysis (PNA). When we apply PNA, we effectively substitute the subsurface conductivity structure by an anisotropic model. In other
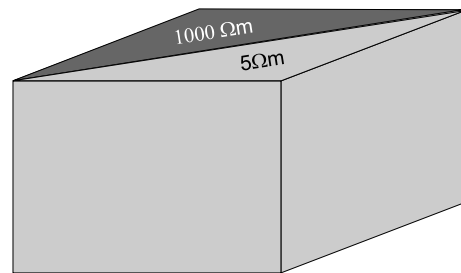

Figure 3. Model of a simple 2-D conductivity contrast striking 45°.
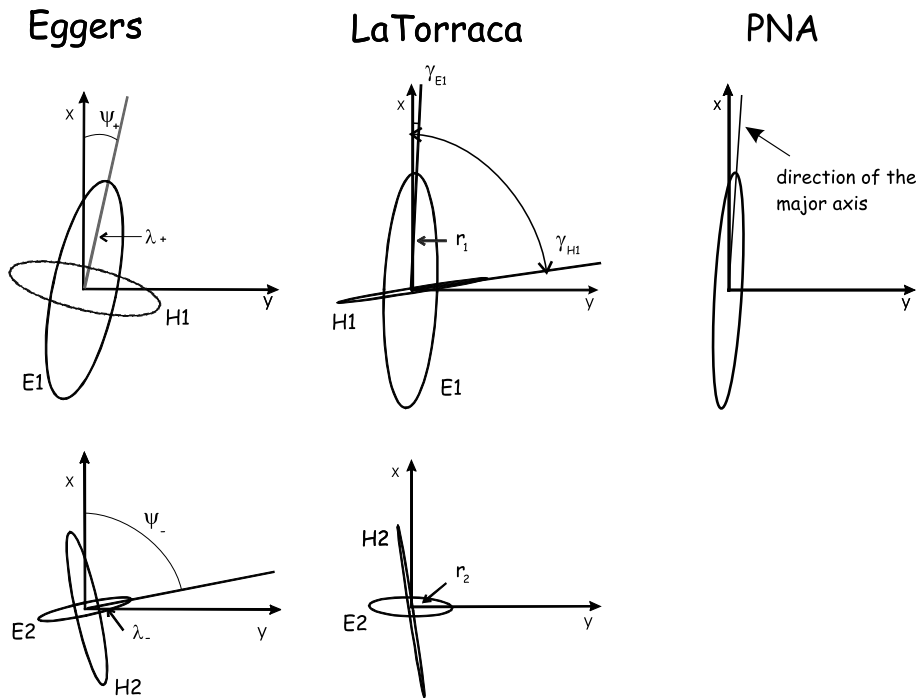

Figure 2. The impedance tensor of eq. (20) is plotted for Eggers' method, the LaTorraca SVD and PNA. The magnetic field amplitude is always unity. Note, that we obtain only one apparent resistivity ellipse with PNA, which is related to the electric field. ($\lambda, r \doteq$ eigenvalues; $\Psi, \gamma \doteq$ principal axis directions).

words, at each frequency of the measured impedance tensor we seek a homogeneous anisotropic subsurface that generates the same impedance tensor. We thereby transform the contrasts and strike directions of conductivity anomalies into their equivalent amounts and directions of anisotropy. It is important to understand that we do not attempt to model an anisotropic crust for the Earth with PNA. We use anisotropy only as a tool to resolve both the conductivity and geometry of an anomaly. However, in the presence of a truly anisotropic subsurface we can likewise image this anisotropy in terms of its strike.

Appendix B outlines a proof demonstrating that PNA truly recovers an arbitrary horizontal anisotropy from the electric and magnetic fields in a chosen coordinate system.

For the graphical representation of the resistivity tensor we use ellipses following the notation of Bibby (1986). Each tensor is split into its symmetric and asymmetric parts, Π_1 and Π_2, respectively:

$$\Pi_1 = \frac{1}{2}\left[(\varrho_{11} - \varrho_{22})^2 + (\varrho_{12} + \varrho_{21})^2\right]^{1/2} \qquad (16)$$
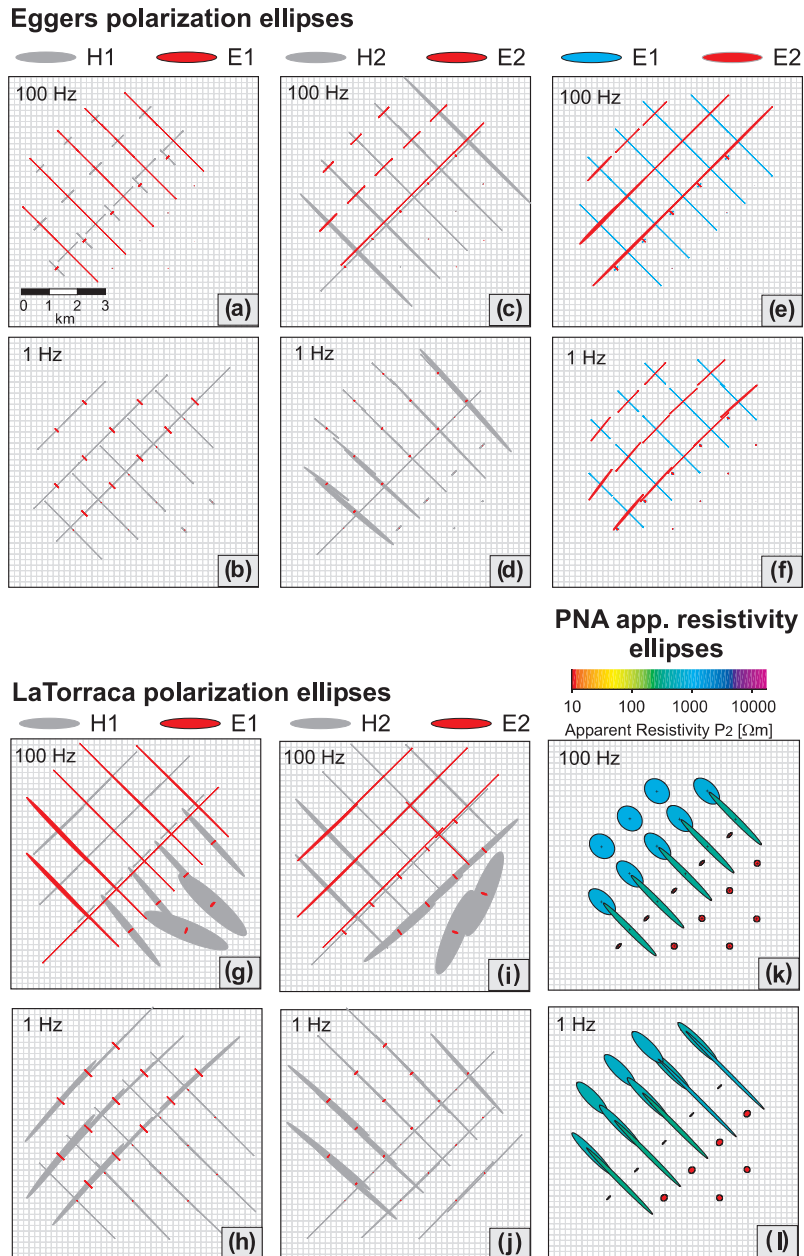

Figure 4. The upper left-hand panel [(a), (b)] shows the first set of Eggers' polarization ellipses (eigenvectors) at frequencies of 100 and 1 Hz. The second set [(c), (d)] at both frequencies is displayed in the middle panel. Both sets clearly indicate the conductivity contrast. Electric and magnetic eigenvectors are orthogonal by definition. A presentation of both electric polarization ellipses [(e), (f)] provides therefore a more comprehensive image of the subsurface. The first set of LaTorraca's polarization ellipses [(g), (h)] maps the conductivity contrast well. By definition the magnetic eigenvectors and the electric eigenvectors are orthogonal, so that the second set of polarization ellipses [(i), (j)] does not provide additional information. The apparent resistivity ellipses [(k), (l)] show a more comprehensive image of the model, as only the shape and direction of one ellipse has to be interpreted. Furthermore, the colour code gives a good estimate of the conductivity of the subsurface.

$$\Pi_2 = \frac{1}{2} \left[(\varrho_{11} + \varrho_{22})^2 + (\varrho_{12} - \varrho_{21})^2 \right]^{1/2} \tag{17}$$

$$\alpha = \frac{1}{2} \arctan \left(\frac{\varrho_{12} + \varrho_{21}}{\varrho_{11} - \varrho_{22}} \right) \tag{18}$$

$$\beta = \frac{1}{2} \arctan \left(\frac{\varrho_{12} - \varrho_{21}}{\varrho_{11} + \varrho_{22}} \right). \tag{19}$$

Fig. 1 shows that the principal axes of a tensor ellipse are expressed as combinations of Π_1 and Π_2. The parameters Π_1 and Π_2 and the angle β are rotationally invariant quantities of the resistivity tensor. The angle α which determines the orientation of the ellipse is not rotationally invariant and thus represents the reference (measurement) coordinate system. Because the ellipses are plotted on top of a site location map (see Fig. 13 in Section 5, for example) with the y-axis in a northerly direction, the reference frame agrees with the geographic coordinate system.

3 COMPARISON BETWEEN PNA, EGGERS' EIGENSTATE ANALYSIS AND LATORRACA SVD

Eggers' eigenstate analysis (Eggers 1982) and LaTorraca's singular-value decomposition (LaTorraca *et al.* 1986) have both been used to analyse the MT impedance. Both methods result in two magnetic and two electric eigenvectors, and two eigenvalues. From these quantities, a total of four polarization ellipses can be constructed: a major (H1) and minor (H2) magnetic and a major (E1) and minor (E2) electric polarization ellipse. Similar to PNA, both methods use the complete impedance tensor information and also use ellipses for graphical presentation.

Eq. (20) shows an example impedance tensor, which Eggers introduced to illustrate his polarization ellipses. Since then, this example tensor has been frequently cited (e.g. LaTorraca *et al.* 1986) and we also use it to compare the three methods in Fig. 2:

$$\hat{\mathbf{Z}} = \begin{pmatrix} 0.097 + 0.208i & 1.140 + 0.957i \\ -0.274 - 0.457i & 0.297 - 0.138i \end{pmatrix}. \tag{20}$$

Using the graphical presentation for tensors, as shown in Fig. 1, we obtain only one ellipse for PNA. Because resistivity (or its inverse, conductivity) is related to the electric field, the apparent resistivity ellipse is comparable to the major electric polarization ellipses (E1) of the other two methods. To demonstrate the full potential of PNA, we test and compare all methods with real and synthetic 3-D data in the next sections.

4 APPLICATION OF PNA TO SYNTHETIC DATA

4.1 2-D synthetic example

We demonstrate the general behaviour of resistivity ellipses using the model shown in Fig. 3. The model comprises two quarter spaces of 1000 and 5 Ωm striking at 45°. Although the conductivity distribution is 2-D, we calculated the model using the 3-D forward modelling code from Mackie *et al.* (1993) and generated an array of stations, evenly distributed on a grid, with a site spacing of approximately 2000 m. For all models described here, we have chosen a grid with 80 horizontal cells in each direction and 35 vertical cells. The horizontal cell is approximately 50–100 m in the vicinity of the conductivity contrast. The central part of the model has a depth

extent of 60 km and is underlain by a homogeneous half-space of 100 Ωm.

After calculation of the full 3-D impedance tensors at two different frequencies (100 and 1 Hz), we applied Eggers', LaTorraca's and PNA methods. The results are compared in Fig. 4 in the form of polarization and apparent resistivity ellipses. For the 2-D case, the polarization ellipses as defined by Eggers and LaTorraca appear as thin lines, which are aligned parallel or perpendicular to the conductivity contrast. The upper left-hand column of Fig. 4 shows Eggers' first set of electric and magnetic polarization ellipses at both frequencies. The lengths of the ellipses are dependent on frequency, but in general, the electric ellipses above the poor conductor are perpendicular to the contrast, while they are aligned in parallel on top of the good conductor. Magnetic and electric ellipses are orthogonal by definition. For the 2-D case, the second set of eigenvectors, and therefore polarization ellipses, are perpendicular to the first one (Figs 4c and d). The angle between major axes of the electric polarization ellipses provides the most useful information concerning the structure of the anomalies. A combination of both electric ellipses, which is plotted on the upper right-hand side of Fig. 4, is therefore adequate for gathering information on the dimensionality and strike direction of the subsurface. This method of presentation also avoids scaling difficulties that arise because the sizes of magnetic and electric polarization ellipses depend strongly on frequency.

LaTorraca's polarization ellipses in Figs 4(g) and (h) appear to be comparable to Eggers' ellipses. Because LaTorraca's method is not restricted to orthogonal electric and magnetic fields, the presentation of the first set of polarization ellipses is already an indication of the geometry of the subsurface. In the case of a 2-D conductivity contrast, the angle between electric and magnetic ellipses is 90°. We would expect to see this behaviour at all frequencies due to the self-similarity of the model. However, at 100 Hz we observe unstable ellipses above the conductive side of the model. This is a numerical artefact already reported by LaTorraca *et al.* (1986). The first and second set of eigenvectors are orthogonal by definition and therefore, the ellipses in Figs 4(i) and (j) contains no additional information.

So far we have seen that both methods can be used to image the strike angle of a (simple) conductivity contrast, but without any indication of the subsurface conductivity. The images show that the
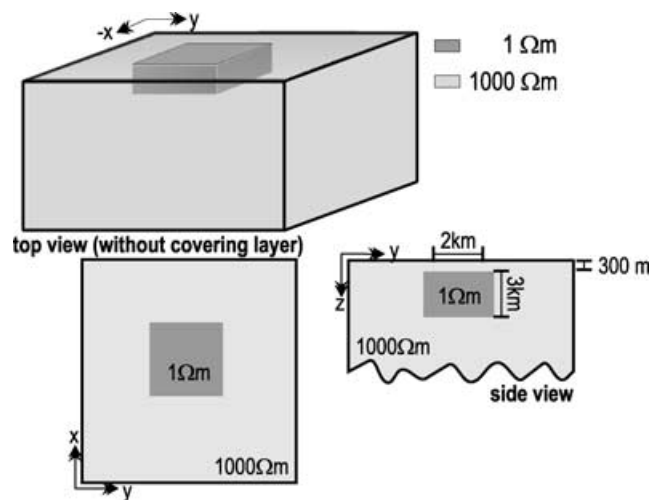
Figure 5. 3-D model of a conductive block (1 Ωm) embedded in a resistive host (1000 Ωm).
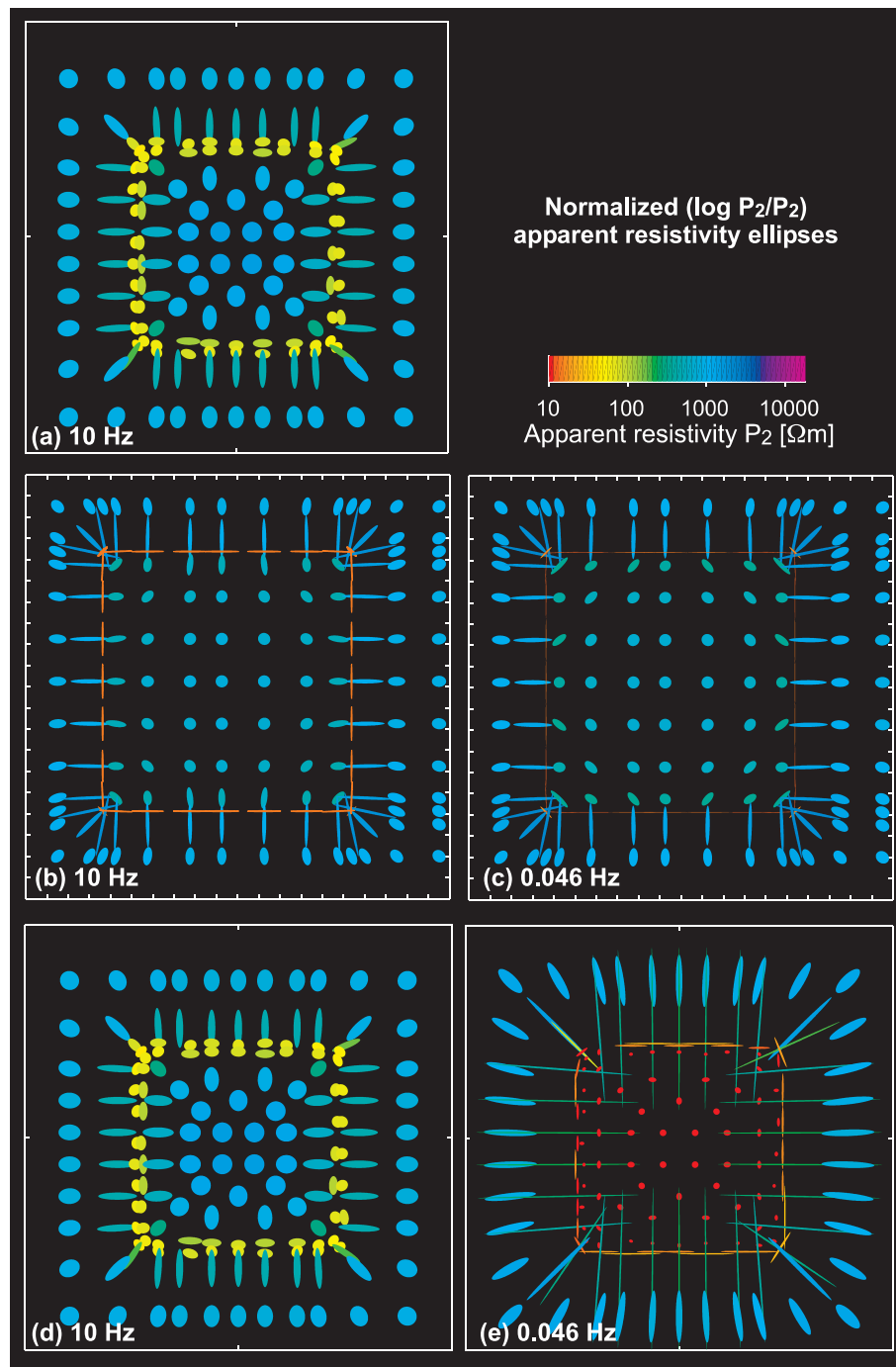
Figure 6. (a) Apparent resistivity ellipses for a station array above the conductive block (see Fig. 5) at 10 Hz. The light green ellipses clearly indicate the dimensions the block. Also a first impression of the conductivity is possible. (b) and (c) Apparent resistivity ellipses for a station array above the conductive ring (see Fig. 7) at 10 and 0.046 Hz. The extremely elongated ellipses in red indicate the conductive frame. The blue and green ellipses represent the resistive host material. For lower frequencies we observe a similar image. (d) and (e) Apparent resistivity ellipses for a station array above the conductive box (see Fig. 11) at 10 Hz and 0.046 Hz. At high frequencies the brim of the box is indicated by yellow ellipses. At a frequency of 0.046 Hz elongated ellipses in red enclose the frame, whereas more circular ellipses in red represent the conductive bottom. We can clearly distinguish that the frame has a bottom.

lengths of the ellipses appear to be dependent upon both the conductivity of the subsurface as well as the site distance from the conductivity contrast. With PNA we retrieve only one ellipse. Its size and orientation are, similarly to the other methods, indicators of the geometry of the conductivity distribution. However, we can gain additional information on the conductivity of the subsurface

by colour coding the ellipses with the determinant of the resistivity tensor (P2). The bottom right-hand corner of Figs 4(k) and (l) shows the apparent resistivity ellipses derived from PNA. Above the poor conductor they are aligned perpendicular to the contact, while above the good conductor they are aligned parallel to it. At some distance from the contrast, dependent on the induction length
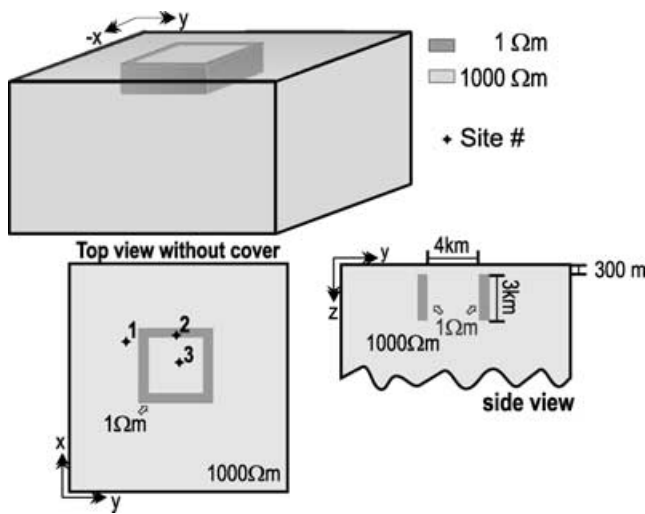
Figure 7. 3-D model of a conductive rectangular ring (1 Ωm) embedded in a resistive host (1000 Ωm). The walls of the conductive frame are 500 m thick.
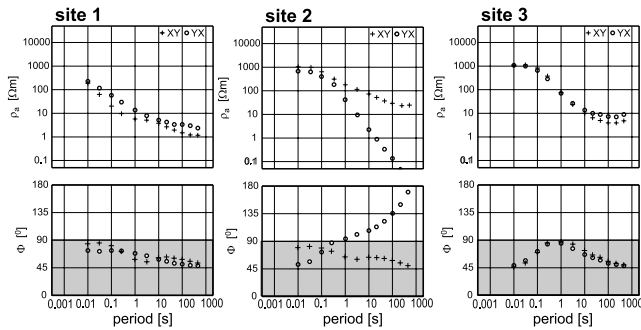

Figure 8. For the ring model we computed ρ_a and phase curves at the three sites marked in Fig. 7. Site 2, which is above the conductive ring exhibits phases above 90°. At sites 1 and 3 inside and outside the ring we do not observe such 3-D effects.

at the particular frequency for the conductivity under consideration, we observe more circular ellipses. For PNA, circular ellipses indicate a 1-D (layered or homogeneous) field distribution. Elongated ellipses are generated close to a conductivity contrast, and generally hint at a 2-D or 3-D field distribution.

4.2 3-D synthetic examples

Now we use the resistivity ellipses to image more complicated conductivity distributions. The next model contains a conductive block of 1 Ωm embedded in a resistive host of 1000 Ωm (Fig. 5). The thickness of the block is 3 km, while the horizontal extent is 2 km. The anomalous block is covered by a 300 m thick layer of resistive host material. Fig. 6(a) shows an image of the resistivity ellipses at a frequency of 10 Hz. The light green and yellow ellipses clearly follow the extensions of the conductive block. Close to all four boundaries, we observe elongated ellipses, while more circular ones are imaged towards the centre of the anomaly and at some distance from the block. The colours of the ellipses reflect resistive and conductive parts of the model.

For the next model we turn the anomalous block into a rectangular frame of conductive material (see Fig. 7).

All other dimensions and the conductivity contrast remain the same. Above the edges of the conductive frame we used a dense
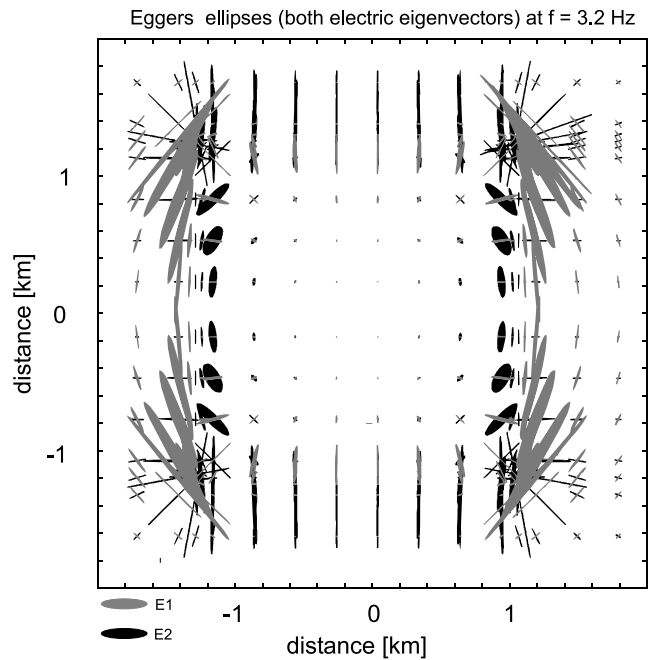

Figure 9. Image of the conductive ring model obtained by Eggers' electric polarization ellipses at 10 Hz: without knowledge of the true conductivity distribution, it is difficult to recover the conductive ring model.
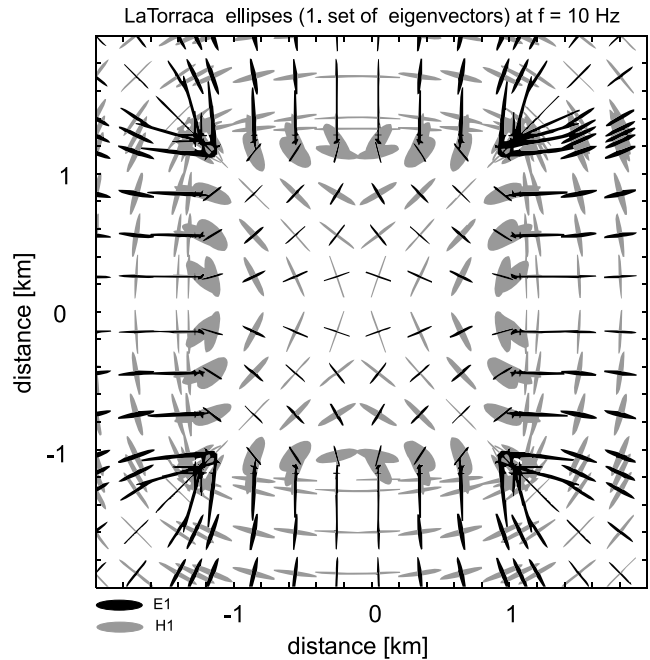

Figure 10. LaTorraca's polarization ellipses reflect the symmetry of the ring model. We obtain the image of a rectangular conductivity anomaly, but it is hard to resolve the thickness of the sides of the box.

grid of 25–50 m cell length for the forward calculations. An image of the apparent resistivity ellipses for this ring model is shown in Fig. 6 for frequencies of 10 Hz (b) and 0.046 Hz (c). At the higher frequency the conductive ring is imaged by extremely elongated red ellipses, whereas green and less elongated ellipses are observed at some distance from the conductivity contrast. PNA delivers a very focused image of the given structure and conductivity distribution. At the lower frequency the image looks quite similar, which
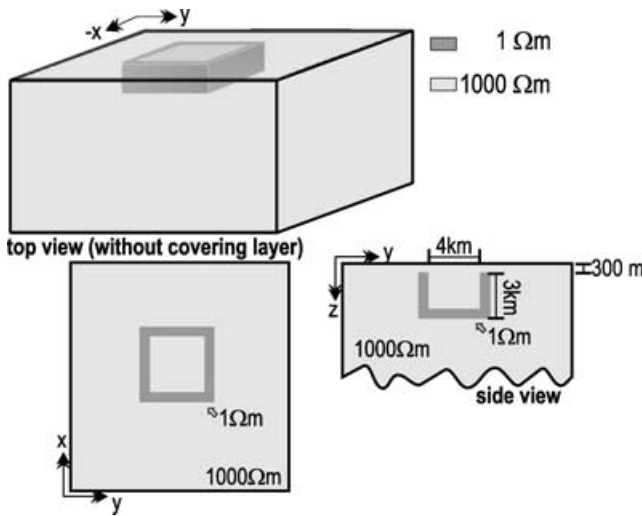
Figure 11. 3-D model of a conductive open box with bottom (1 Ωm) in a resistive host (1000 Ωm). The thickness of the bottom and the walls is again 500 m.

Figure 12. Presentation of the error bounds for a resistivity ellipse. The extremal orientations of the major axis are marked by two lines. The ticks indicate the maximum and minimum elongation of the major axis with respect to the data error.

indicates that long-period data might also be effected by shallow anomalies.

Fig. 7 shows the locations of three sites for which the apparent resistivity and phase curves are plotted in Fig. 8. All the sites located above or in close vicinity to the conductive ring show phase values exceeding 90°. Site 2 is representative of this behaviour, which is a clear indication of a strongly 3-D field distribution. The sounding curves at site 1 and site 3, on the other hand, indicate that the 3-D effects are very local, concentrated directly above the ring. Nevertheless, PNA seems to produce stable and meaningful results even under these circumstances. Fig. 9 displays Eggers' polarization ellipses of both electric eigenvectors at a frequency of 10 Hz. The image is almost incomprehensible as it is impossible to recognize a rectangular conductivity anomaly. In contrast, the first set of LaTorraca's polarization ellipses image the expected rectangular anomaly. The general trend of the electric polarization ellipses is similar to that of the apparent resistivity ellipses. However, the resistivity ellipses provide a much better impression of the thickness of the conductor. From the LaTorraca ellipses alone, it is hard to conclude whether the object is a solid block or a conductive ring.

Fig. 11 shows the model of a conductive box (open), buried in a resistive host. All dimensions and conductivity contrasts remain the same but now the ring is closed by a conductive bottom at a depth of 3.3 km. Figs 6(d) and (e) shows the apparent resistivity ellipses for this model, again at frequencies of 10 and 0.046 Hz. As expected, we observe the image of a conductive rectangular ring at higher frequencies (10 Hz). At lower frequencies (greater penetration depth), the brim of the box is imaged by elongated red ellipses but now, the conductive bottom of the box becomes visible. It is expressed by the red circular ellipses inside the box.

5 APPLICATION OF PNA TO THE MT DATA SET FROM NAMIBIA

The above 3-D modelling studies illustrate both the capability of PNA to image complicated 3-D MT data and the importance of dense measurements in order to interpret ellipse plots. To apply PNA to field data, we chose a set of MT data from Namibia (Ritter *et al.* 2003; Weckmann *et al.* 2003). The data were recorded
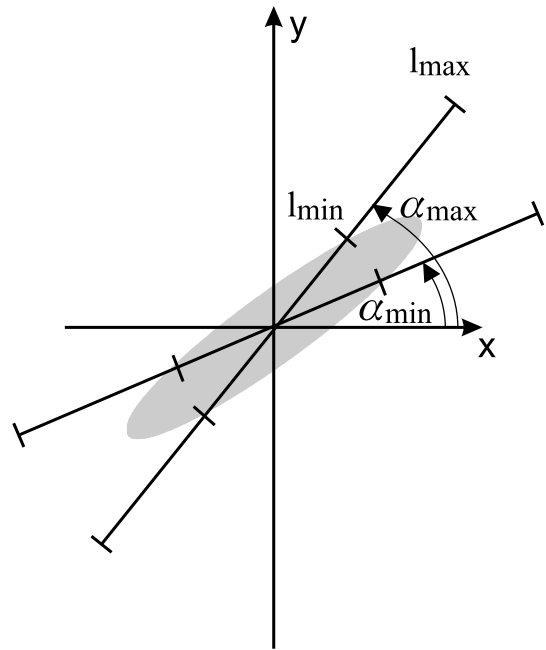
at 60 sites with a site spacing of 500 and 2000 m across the Waterberg Fault/Omaruru Lineament (WF/OL), a major fault zone within the Damara Belt. In the vicinity of the WF/OL we observe strong 3-D effects, especially at long periods: very high skew, phases over 90° and three large (and one poorly determined) apparent resistivity components. In conjunction with real data it is important to show not only the resistivity ellipses but also their error margins. The latter demonstrate how stable and reliable the obtained ellipses are, when the transfer functions contain error bars. Developing rigorous error propagation for PNA is quite complicated, instead we follow a different approach: within the error bounds of each impedance tensor element, we computed a set of 500 random impedance tensor elements. Each individual tensor element is plotted in the complex plane to verify that a regular distribution of impedance estimates within their error margins is achieved. In such a map the error bound forms a circle around the complex tensor element. Subsequently, PNA is applied to each impedance tensor and the length and the angle of the major axis of the ellipse are computed. As a next step, we determine the minimum and maximum lengths as well as the minimum and maximum angles of the major axis. Fig. 12 shows an example of a resistivity ellipse together with its error margins. Minimum and maximum angles of the major axis are indicated by two lines, while tick marks denote the minimum and maximum elongation of the ellipses.

The resistivity ellipses of all sites in the Namibia data set are plotted in Figs 13(a)–(c) at three different frequencies. The location of the WF/OL is indicated in Fig. 13(b). At the highest frequency we observe elongated ellipses in the northern part of the profiles, whereas the ellipses in the southern part are less elongated. This behaviour is most distinct at 5.56 Hz where less elongated ellipses south of the WF/OL are orientated almost NS. At most sites north of the fault elongated ellipses can be observed. The orientation and shape of the ellipses indicate that the region to the north of the WF/OL consists of either a NNE–SSW-trending conductivity anomaly or an
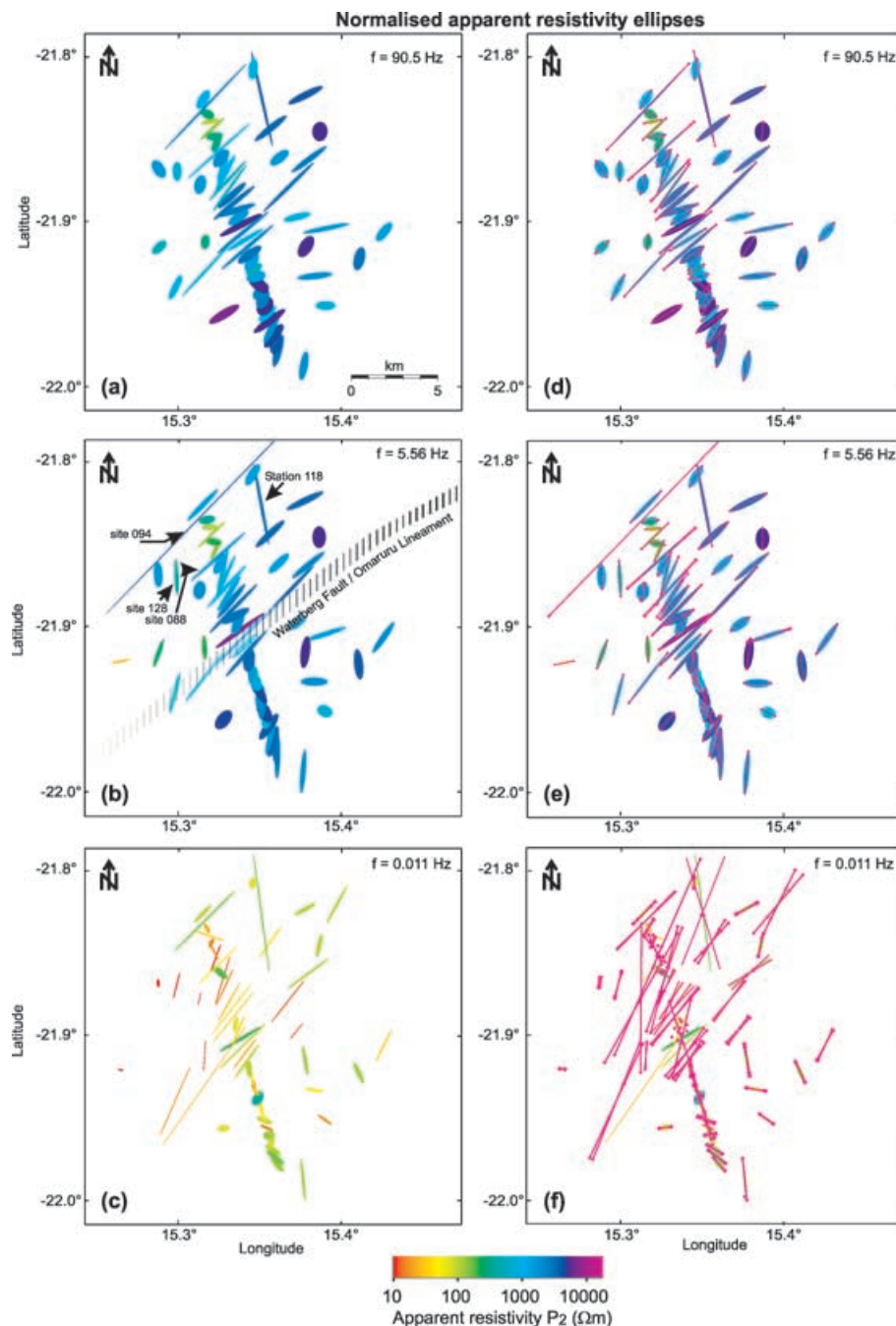
Figure 13. (a)–(c) Resistivity ellipses at three different frequencies for the MT data from Namibia. They indicate the location of the Waterberg Fault/Omaruru Lineament by a change in shape and orientation of the resistivity ellipses. The colour code indicates a resistive subsurface at high frequencies (90.5 and 5.56 Hz) and high conductivity at low frequencies (0.011 Hz). (d)–(f) The same ellipses overlain by error bounds for the resistivity ellipses at the same frequencies. At high frequencies where we observe vanishing data errors as the two error lines coincide. The MT impedances at low frequencies (f) have considerable data errors, but they generate only small deviations in the orientation and shape of the resistivity ellipses.

anisotropic region with enhanced conductivity parallel to the fault. Sites 118, 094, 128 and 088, which are marked in Fig. 13(b), are located on a conductive ring structure (see Weckmann *et al.* 2003). Their resistivity ellipses are extremely elongated and appear to follow this structure, which is comparable to the 3-D modelling results of the conductive box (see Fig. 8). At frequencies >5 Hz, the colours of the ellipses indicate a resistive shallow crust. However, at 0.011 Hz the orientations of the ellipses remain the same, but their colours reflect higher conductivity at greater depths. The right-hand column

of Fig. 13 shows the resistivity ellipses at the same frequencies, but now with error margins. At the two highest frequencies both error lines as well as the minimum and maximum elongation coincide, indicating the vanishing error margins of the impedance estimates. At low frequencies, we observe phases over 90° and one poorly determined off-diagonal tensor element, which translates into larger errors for the ellipses. This observation demonstrates that PNA is robust and hence particularly useful for application to real data. A more complete interpretation of the data set based on 3-D and 2-D

anisotropic modelling and the geodynamic implications are given in Weckmann *et al.* (2003) and Ritter *et al.* (2003).

6 DISCUSSION

In order to make use of the tensor properties of the derived resistivity tensor, we choose invariants for presenting the resistivity tensor. A review of the meaning of impedance tensor invariants is not the goal of this work, but many papers have already dealt with their presentation and interpretation. Weaver *et al.* (2000) and Szarka & Menvielle (1997) propose the analysis of the seven invariants as a suitable method for imaging conductivity distributions and classifying distortion and dimensionality. The authors present invariants in the form of contour maps in the surface plane for a specific frequency. Weaver *et al.* (2000) demonstrate with synthetic data that a 3-D conductivity distribution can be imaged by invariants, although the relation to depth is difficult. In particular, the first four of invariants from Weaver *et al.* (2000) and Szarka & Menvielle (1997) can reproduce the geometry of the anomalies. However, the invariants are independent of conductivity, in contrast to PNA, where the conductivity of the subsurface can be assessed. In principle, the resistivity tensor derived by PNA could be displayed and analysed similarly in the form of contour plots. A major disadvantage of this approach though is that a dense regular station array is necessary to avoid interpolation or gridding effects. This is possible for synthetic MT data, but is difficult to achieve with the sparse and irregular spacing of real data. The presentation of the resistivity tensor in the form of ellipses overcomes this obstacle. Because the ellipses are plotted only at the site locations it is clearly shown where data and information are available. Additionally, with ellipses, the information of several aspects of the apparent resistivity tensor can be condensed into one meaningful parameter.

Weaver *et al.* (2000) discuss that three of their invariants can be compared with the galvanic distortion parameters twist and shear (Groom & Bailey 1989). Although PNA is not regarded as a tensor decomposition tool, we tested the influence of galvanic distortion by multiplying the example impedance tensor (see eq. 20) with a real distortion matrix. The distortion resulted mainly in a change of the direction of the main axis, but not in a change of the shape of the ellipses.

7 SUMMARY

We have introduced propagation number analysis as a method for deriving a resistivity tensor from the magnetotelluric impedance. For imaging purposes, the electrical resistivity is a physically meaningful parameter and the tensor characteristics allow the computation of rotationally invariant properties. We have demonstrated the potential of the method in comparison with two existing methods using synthetic 3-D data. The modelling study and the application of PNA to real data show that this method can produce focused images with stable results even if the electromagnetic fields are strongly 3-D. The method and its error estimation can easily be adapted to real data as it does not require any prerequisites. It can be used as an interpretation tool in combination with surface geological maps or as a computationally inexpensive way to obtain a starting model for a 3-D inversion.

The limitations of the method are common to similar imaging tools. The biggest problem is the difficulty in relating the observed images to depth. Because of the skin depth phenomena, the corresponding observation depths are always a function of both frequency and subsurface conductivity and like all imaging methods,

PNA requires a dense station mesh so that images can be obscured or distorted by spatial aliasing.

REFERENCES

Bahr, K., 1991. Geological noise in magnetotelluric data: a classification of distortion types, *Phys. Earth planet. Inter.,* **66,** 24–38.

Bibby, H.M., 1986. Analysis of multiple source bipole–quadrupole resistivity surveys using apparent resistivity tensor, *Geophysics,* **51,** 972–983.

Caldwell, T.G. & Bibby, H.M., 1998. The instantaneous apparent resistivity tensor: a visualization scheme for lotem electric field measurements, *Geophys. J. Int.,* **135,** 817–834.

Caldwell, T.G., Bibby, H.M. & Reilly, W.I., 1998. Visualisation of 3D magnetotelluric data using apparent resistivity and apparent permittivity tensors, *14th Workshop on Electromagnetic Induction in the Earth*, Sinaia, Romania.

Eggers, D.E., 1982. An eigenstate formulation of the magnetotelluric impedance tensor, *Geophysics,* **47,** 1204–1214.

Fischer, G. & Masero, W., 1994. Rotational properties of the magnetotelluric impedance tensor: the example of the Araguainha impact crater, Brazil, *Geophys. J. Int.,* **119,** 548–560.

Groom, R.W. & Bailey, R.C., 1989. Decomposition of magnetotelluric impedance tensors in presence of local three-dimensional galvanic distortion, *J. geophys. Res.,* **94,** 1913–1925.

LaTorraca, G.A., Madden, T.R. & Korringa, J., 1986. An analysis of the magnetotelluric impedance for three-dimensional conductivity structures, *Geophysics,* **51,** 1819–1829.

Lezaeta, P. & Haak, V., 2003. Beyond MT decomposition: current channeling and magnetotelluric phases over 90°, *J. geophys. Res.,* **108,** 36, 2305, doi: 10.1029/2001 JB 000 990.

Lilley, F.E.M., 1993. Magnetotelluric analysis using Mohr circles, *Geophysics,* **58,** 1498–1506.

Mackie, R.L., Madden, T.R. & Wannamaker, P.E., 1993. Three-dimensional magnetotelluric modelling using difference equations—theory and comparisons to integral equation solutions, *Geophysics,* **58,** 215–226.

McNeice, G.W. & Jones, A.G., 2001. Multisite, multifrequency tensor decomposition of magnetotelluric data, *Geophysics,* **66,** 158–173.

Negi, J.G. & Saraf, P.D., 1989. *Anisotropy in Geoelectromagnetism, Methods in Geochemistry and Geophysics,* Vol. 28, Elsevier, Amsterdam.

Reilly, W.I., 1979. Anisotropy tensors in magnetotelluric application, *Technical Report,* Department of Scientific and Industrial Research, New Zealand, Wellington.

Ritter, O., Weckmann, U., Vietor, T. & Haak, V., 2003. A magnetotelluric study of the Damara Belt in Namibia. Part I: regional scale conductivity anomalies, *Phys. Earth planet. Inter.,* **138,** 71–90, doi: 10.1016/50031-9201 (03) 00078-5.

Smith, J.T., 1995. Understanding telluric distortion matrices, *Geophys. J. Int.,* **122,** 219–226.

Swift, C., 1967. A magnetotelluric investigation of an electrical conductivity anomaly in the southwestern United States, *PhD thesis,* MIT, Cambridge, MA.

Szarka, L. & Menvielle, M., 1997. Analysis of rotational invariants of the magnetotelluric impedance tensor, *Geophys. J. Int.,* **129,** 133–142.

Weaver, J.T., Agarwal, A.K. & Lilley, F.E.M., 2000. Characterization of magnetotelluric tensor in terms of its invariants, *Geophys. J. Int.,* **141,** 321–336.

Weckmann, U., Ritter, O. & Haak, V., 2003. A magnetotelluric study of the Damara Belt in Namibia. Part II: MT phases over 90° reveal the internal structure of the Waterberg Fault/Omaruru Lineament, *Phys. Earth planet. Inter.,* **138,** 91–112, doi: 10.1016/50031-9201 (03) 00079-1.

APPENDIX A: WHEN DOES A MATRIX CORRESPOND TO A TENSOR?

What are the differences between tensors and matrices? We attempt to give a concept, not a mathematically rigorous proof. Generally speaking, a matrix corresponds to a tensor if the following two procedures lead to the same result (see Fig. A1):

  (i) Establishing the tensor in a given coordinate system and subsequent transformation into a second coordinate system.
  (ii) Transformation of the tensor elements into the second coordinate system and subsequent establishment of the tensor.

To apply this concept to the ρ_a matrix, we first rotate the impedance tensor. Subsequently, the apparent resistivity values are calculated. For simplicity, we rotate a 2-D impedance tensor by angle θ.

$$\hat{Z}' = \begin{pmatrix} \cos\theta & \sin\theta \\ -\sin\theta & \cos\theta \end{pmatrix} \begin{pmatrix} 0 & Z_\perp \\ Z_\parallel & 0 \end{pmatrix} \begin{pmatrix} \cos\theta & -\sin\theta \\ \sin\theta & \cos\theta \end{pmatrix}. \tag{A1}$$

The first two elements of the rotated impedance tensor are

$$Z'_{xx} = \frac{1}{2}(Z_\perp + Z_\parallel)\sin(2\theta)$$
$$Z'_{xy} = \frac{1}{2}(Z_\perp - Z_\parallel) + \frac{1}{2}(Z_\perp + Z_\parallel)\cos(2\theta). \tag{A2}$$

The elements of the apparent resistivity matrix are derived by taking the absolute values squared of the impedance tensor elements. The matrix is then rotated similarly to eq. (A1)

$$\rho'_a = \frac{\mu_0}{2\pi f}\begin{pmatrix} \cos\theta & \sin\theta \\ -\sin\theta & \cos\theta \end{pmatrix} \begin{pmatrix} 0 & |Z_\perp|^2 \\ |Z_\parallel|^2 & 0 \end{pmatrix} \begin{pmatrix} \cos\theta & -\sin\theta \\ \sin\theta & \cos\theta \end{pmatrix} \tag{A3}$$

and the elements of ρ_a take the following form:

$$\rho'_{a,xx} = \frac{\mu_0}{2\pi f}\left[\frac{1}{2}\left(|Z_\perp|^2 + |Z_\parallel|^2\right)\sin(2\theta)\right]$$
$$\rho'_{a,xy} = \frac{\mu_0}{2\pi f}\left[\frac{1}{2}\left(|Z_\perp|^2 - |Z_\parallel|^2\right) + \frac{1}{2}\left(|Z_\perp|^2 + |Z_\parallel|^2\right)\cos(2\theta)\right]. \tag{A4}$$

If ρ_a is a tensor, then

$$\frac{\mu_0}{2\pi f}|Z'_{ij}|^2 \overset{?}{=} \rho'_{a,ij} \tag{A5}$$

with $i, j = x, y$. $\rho'_{a,ij}$ are summation terms of absolute values squared of $Z_\parallel$ or $Z_\perp$. Hence, ρ_a is generally *not* a tensor because $|a + b| \leq |a| + |b|$.

To decide if $\hat{\gamma}$ is a tensor, we must rotate the admittance tensor $\hat{Y}$ into a second coordinate system and then calculate $\hat{\gamma}$. The rotated admittance tensor assumes the following form when we consider some substitutions for sums and differences of admittance tensor entries: $S_1 = Y_{xx} + Y_{yy}$, $S_2 = Y_{xy} + Y_{yx}$, $D_1 = Y_{xx} - Y_{yy}$ and $D_2 = Y_{xy} - Y_{yx}$:

$$\hat{Y}' = \begin{pmatrix} \cos\theta & \sin\theta \\ -\sin\theta & \cos\theta \end{pmatrix} \begin{pmatrix} Y_{xx} & Y_{xy} \\ Y_{yx} & Y_{yy} \end{pmatrix} \begin{pmatrix} \cos\theta & -\sin\theta \\ \sin\theta & \cos\theta \end{pmatrix}$$
$$= \frac{1}{2}\begin{pmatrix} S_1 + D_2\cos(2\theta) + S_2\sin(2\theta) & D_2 + S_2\cos(2\theta) - D_1\sin(2\theta) \\ -D_2 + S_2\cos(2\theta) - D_1\sin(2\theta) & S_1 - D_1\cos(2\theta) - S_2\sin(2\theta) \end{pmatrix}. \tag{A6}$$

Considering one element, e.g. γ_{xy}, we derive an analogue to eq. (A6),

$$\gamma_{xy}(\alpha) = \frac{1}{2}[(\gamma_{xy} - \gamma_{yx}) + (\gamma_{xy} + \gamma_{yx})\cos(2\theta) - (\gamma_{xx} - \gamma_{yy})\sin(2\theta)]$$

$$= -\frac{\omega^2}{2}\left\{[Y_{yy}(Y_{xy} - Y_{yx}) - Y_{xx}(Y_{yx} - Y_{xy})] + [Y_{yy}(Y_{xy} - Y_{yx}) + Y_{xx}(Y_{yx} - Y_{xy})]\cos(2\alpha)\right.$$
$$\left. - \left[\left(Y_{yy}Y_{xx} - Y_{yx}^2\right) - Y_{yy}Y_{xx} - Y_{xy}^2\right]\sin(2\alpha)\right\}$$

$$= -\frac{\omega^2}{2}[D_2 S_1 - D_2 D_1\cos(2\alpha) - D_2 S_2\sin(2\alpha)]$$

$$= -\frac{\omega^2}{2}D_2[S_1 - D_1\cos(2\alpha) - S2\sin(2\alpha)]$$

$$= -\omega^2 Y_{y'y'}(\alpha)[Y_{x'y'}(\alpha) - Y_{y'x'}(\alpha)] = \gamma_{x'y'}. \tag{A7}$$

q.e.d.

APPENDIX B: CAN PNA RECOVER ARBITRARY ANISOTROPY?

To test if the propagation number analysis properly recovers the conductivity tensor of an arbitrary horizontally anisotropic, homogeneous medium in the chosen coordinate system, we describe the subsurface by a conductivity tensor for which principal axes are rotated by the angle β from the geographical coordinate system (see Fig. B1).
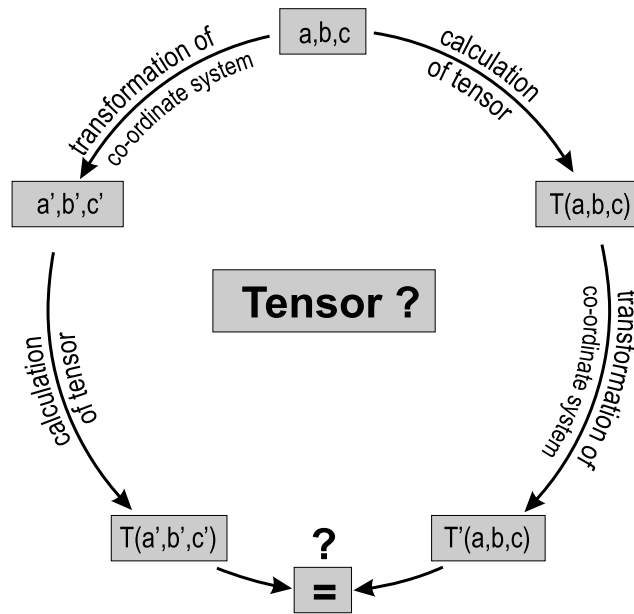
Figure A1. Examination of tensor properties: a quantity depending on a, b and c is defined in a coordinate system (x, y, z). It must be shown that $T(a', b', c') = T'(a, b, c)$.

At first we have to compute the electric and magnetic fields, which generate the admittance tensor. The wave equation for the electric fields in the case of azimuthal anisotropy and neglecting the displacement currents has the following form:

$$\frac{\partial^2 E_x}{\partial z^2} = i\omega\mu_0(\sigma_{xx}E_x + \sigma_{xy}E_y)$$

$$\frac{\partial^2 E_y}{\partial z^2} = i\omega\mu_0(\sigma_{yx}E_x + \sigma_{yy}E_y),$$

(B1)

where $\sigma_{xy} = \sigma_{yx}$ and E_x, E_y only depend on the depth z. To solve these equations we assume a plane-wave solution:

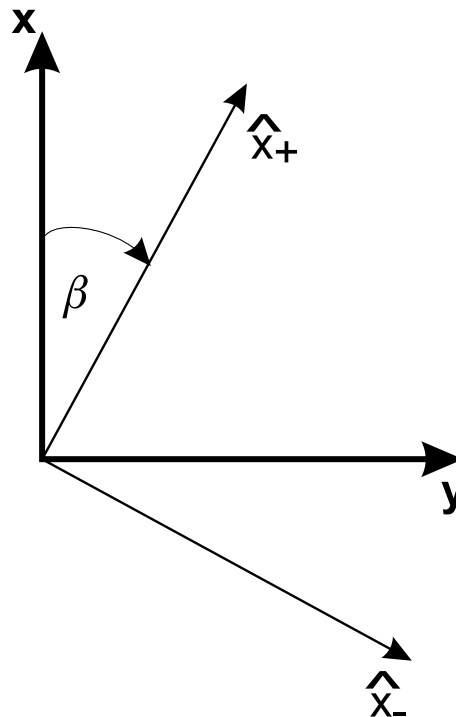$$E_x(z) = A_1 e^{-kz} \quad E_y(z) = A_2 e^{-kz}$$

(B2)

Figure B1. Conductivity tensor in a geographic coordinate system. $\hat{x}_+$ and $\hat{x}_-$ are the unit vectors of the conductivity tensor, which is rotated by β from the geographic coordinate system.

with the complex wavenumber $k = \sqrt{i\omega\mu_0\sigma}$. For this expression we need the eigenvalue of σ. Combining eqs (B2) and (B1) we obtain

$$\sigma A_1 = \sigma_{xx} A_1 + \sigma_{xy} A_2$$
$$\sigma A_2 = \sigma_{xy} A_1 + \sigma_{yy} A_2. \tag{B3}$$

If a solution of the equation system exists, the eigenvalue σ must be

$$\Rightarrow \sigma = \sigma_\pm = \frac{1}{2}\left[\sigma_{xx} + \sigma_{yy} \pm \sqrt{(\sigma_{xx} - \sigma_{yy})^2 + 4\sigma_{xy}^2}\right]. \tag{B4}$$

Using Vieta's theorem we can define

$$\sigma_+ + \sigma_- = \sigma_{xx} + \sigma_{yy}; \qquad \sigma_+ \cdot \sigma_- = \sigma_{xx}\sigma_{yy} - \sigma_{xy}^2. \tag{B5}$$

We can transform eq. (B3) into

$$\frac{A_2^\pm}{A_1^\pm} = \frac{\sigma_\pm - \sigma_{xx}}{\sigma_{xy}} = \frac{\sigma_{xy}}{\sigma_\pm - \sigma_{yy}} = \tan\beta \tag{B6}$$

using the geometric relations of Fig. 15.

To compute the admittance tensor (2) we consider two polarizations:

(a) $A_j^+ \neq 0$ and $A_j^- = 0$

(b) $A_j^- \neq 0$ and $A_j^+ = 0$ with $j = x, y$.

The magnetic field is given by Faraday's law (3),

$$B_x^\pm = -\frac{k^\pm}{i\omega} E_y; \quad B_y^\pm = \frac{k^\pm}{i\omega} E_x = \sqrt{\frac{\mu_0 \sigma_\pm}{i\omega}} E_x. \tag{B7}$$

Together with

$$\hat{Y} =: \frac{\sqrt{i\omega\mu_0}}{i\omega}\widetilde{Y} = \sqrt{\frac{\mu_0}{i\omega}}\widetilde{Y} \tag{B8}$$

the conditional equation for $\widetilde{Y}_{xx}$ and $\widetilde{Y}_{xy}$ can be written as

$$-\sqrt{\sigma_\pm} A_2^\pm = \widetilde{Y}_{xx} A_1^\pm + \widetilde{Y}_{xy} A_2^\pm. \tag{B9}$$

In consideration of eq. (B6) we have to solve the following system of equations:

$$-\sqrt{\sigma_\pm} = \frac{\sigma_{xy}}{\sigma_\pm - \sigma_{xx}}\widetilde{Y}_{xx} + \widetilde{Y}_{xy}. \tag{B10}$$

With regard to eq. (B6) the determinant of the system is given by

$$\frac{\sigma_{xy}}{\sigma_+ - \sigma_{xx}} - \frac{\sigma_{xy}}{\sigma_- - \sigma_{xx}} = \frac{\sigma_+ - \sigma_-}{\sigma_{xy}}. \tag{B11}$$

Therefore, $\widetilde{Y}_{xx}$ and $\widetilde{Y}_{xy}$ become

$$\widetilde{Y}_{xx} = -\frac{\sigma_{xy}}{\sqrt{\sigma_+} + \sqrt{\sigma_-}}; \qquad \widetilde{Y}_{xy} = -\frac{\sigma_{yy} + \sqrt{\sigma_-\sigma_+}}{\sqrt{\sigma_-} + \sqrt{\sigma_+}}. \tag{B12}$$

Similar considerations lead to expressions for $\widetilde{Y}_{yx}$ and $\widetilde{Y}_{yy}$.

$$\widetilde{Y}_{yx} = \frac{\sigma_{xx} + \sqrt{\sigma_-\sigma_+}}{\sqrt{\sigma_-} + \sqrt{\sigma_+}}; \qquad \widetilde{Y}_{yy} = \frac{\sigma_{xy}}{\sqrt{\sigma_-} + \sqrt{\sigma_+}}. \tag{B13}$$

Now, the admittance tensor can be written as

$$\hat{Y} = \frac{\sqrt{\mu_0/(i\omega)}}{\sqrt{\sigma_-} + \sqrt{\sigma_+}}\begin{pmatrix} -\sigma_{xy} & -(\sigma_{yy} + \sqrt{\sigma_+\sigma_-}) \\ \sigma_{xx} + \sqrt{\sigma_+\sigma_-})\sigma_{xy} & \end{pmatrix}. \tag{B14}$$

This admittance tensor is used to compute the propagation number $\hat{\gamma}$ (eq. 14).

$$\gamma_{ij} = -i\omega\mu_0\sigma_{ij}, \quad \text{with} \quad i, j = x, y. \tag{B15}$$

Hence we have shown that the entries of the propagation number $\hat{\gamma}$ contain the related components of the conductivity tensor in the geographic coordinate system.